Mohammad K. Jawed
Department of Mechanical Engineering,
Massachusetts Institute of Technology,
Cambridge, MA 02139
e-mail: khalidjm@mit.edu

Pierre-Thomas Brun
Department of Mathematics,
Massachusetts Institute of Technology,
Cambridge, MA 02139
e-mail: ptbrun@mit.edu

Pedro M. Reis[1]
Department of Mechanical Engineering,
Massachusetts Institute of Technology,
Cambridge, MA 02139;
Department of Civil and
Environmental Engineering,
Massachusetts Institute of Technology,
Cambridge, MA 02139
e-mail: preis@mit.edu

A Geometric Model for the Coiling of an Elastic Rod Deployed Onto a Moving Substrate

We report results from a systematic numerical investigation of the nonlinear patterns that emerge when a slender elastic rod is deployed onto a moving substrate; a system also known as the elastic sewing machine (ESM). The discrete elastic rods (DER) method is employed to quantitatively characterize the coiling patterns, and a comprehensive classification scheme is introduced based on their Fourier spectrum. Our analysis yields physical insight on both the length scales excited by the ESM, as well as the morphology of the patterns. The coiling process is then rationalized using a reduced geometric model (GM) for the evolution of the position and orientation of the contact point between the rod and the belt, as well as the curvature of the rod near contact. This geometric description reproduces almost all of the coiling patterns of the ESM and allows us to establish a unifying bridge between our elastic problem and the analogous patterns obtained when depositing a viscous thread onto a moving surface; a well-known system known as the fluid-mechanical sewing machine (FMSM). [DOI: 10.1115/1.4031363]

1 Introduction

A slender elastic rod deployed onto a moving substrate can form a variety of geometrically nonlinear periodic patterns [1–3] that are reminiscent of the stitches of a sewing machine. As such, this problem has come to be known as the elastic sewing machine (ESM) [1]. The various patterns have a well-defined wavelength and time period, selected primarily by the speed mismatch between the injection and the moving substrate. This nonlinear scenario arises in a variety of engineering contexts, ranging from the installation of transoceanic cables [4] to the flow-directed fabrication of carbon nanotube serpentines [5].

In the fluid analog of the ESM, a thin thread of viscous fluid is poured onto a moving belt; appropriately named as the fluid-mechanical sewing machine (FMSM) [6]. The FMSM has been investigated more extensively than the ESM, with numerous experimental [6–10], theoretical [11–13], and numerical [14–18] studies. Studies of the ESM, on the other hand, are more recent [1–3]. For the case of a static substrate, the elastic rod typically forms circular coils that have been analyzed numerically [19] and experimentally [20]. The system was extended to include a moving substrate, for which a plethora of patterns have been found [1].

Previously [3], we combined precision model experiments with numerical simulations to quantitatively characterize the coiling patterns of the ESM. The simulations were based on the discrete elastic rod method (DER) [17,21] (a robust and predictive simulation tool that was originally developed by the computer graphics community) and were found to be in excellent agreement with our own experiments. Subsequently [2], we systematically applied DER to further explore the parameter space of this problem and pin-point the paramount role played by geometry. Despite the drastic difference in the constitutive description between the elastic rods of the ESM and the viscous threads of the FMSM, the geometry of the patterns produced by the two systems is strikingly similar. For the case of a viscous thread, a comprehensive description from a geometric perspective has been provided [22], which

suggests that geometry may be the connecting thread between the FMSM and the ESM. These similarities call for a quantitative comparison between the two systems.

Here, we develop a geometric model (GM) to describe the complex coiling patterns obtained in the ESM, which is then used to identify common links with the FMSM. We make use of computer simulations (previously validated against precision experiments [3]) to systematically explore the parameter space and characterize the coiling patterns in detail. Moreover, we provide a rigorous classification scheme of the nonlinear patterns based on the analysis of their Fourier spectrum. Underlying this complexity, we find a remarkably simple description for both the periodicity and the morphology of the patterns. An analogy with a simple pendulum enables us to identify an intrinsic *natural* radius of curvature of the system that dictates the wavelength of all the patterns. Through a geometric construction, we show that the shape and evolution of the patterns with the control parameter can be rationalized with the three same ordinary differential equations (ODEs) that were originally developed for the FMSM [22]. These ODEs offer a mathematical description for the pattern formation process for coiling onto a moving substrate. We compare the phase diagrams of the ESM and FMSM, find many quantitative similarities, and establish a unifying bridge between the two systems.

2 Definition of the Problem

A schematic diagram of our problem is presented in Fig. 1(*a*). A thin elastic rod is deployed vertically from a height H, and at a speed v, onto a rigid substrate (conveyor belt) that translates horizontally at speed v_b. The control parameter of the system is taken to be the dimensionless speed mismatch, $\epsilon = (v - v_b)/v$, between the injector and the belt. The characteristic length scale of the problem is $L_{gb} = [r_0^2 E/(8\rho g)]^{1/3}$, where r_0 is the cross-sectional radius of the rod, E is the Young's modulus, ρ is the density, and g is the gravitational acceleration. This gravito-bending length arises from a balance between elastic bending energy and gravitational potential. Previously, we showed that L_{gb} is the primary ingredient in setting the various length scales of the patterns in a regime where inertia is negligible [3]. Moreover, the deployment height was found to only have a weak logarithmic effect on the pattern length scales [2]. In the numerical simulations performed for the current study, the parameters of the rod were: $r_0 = 0.16$
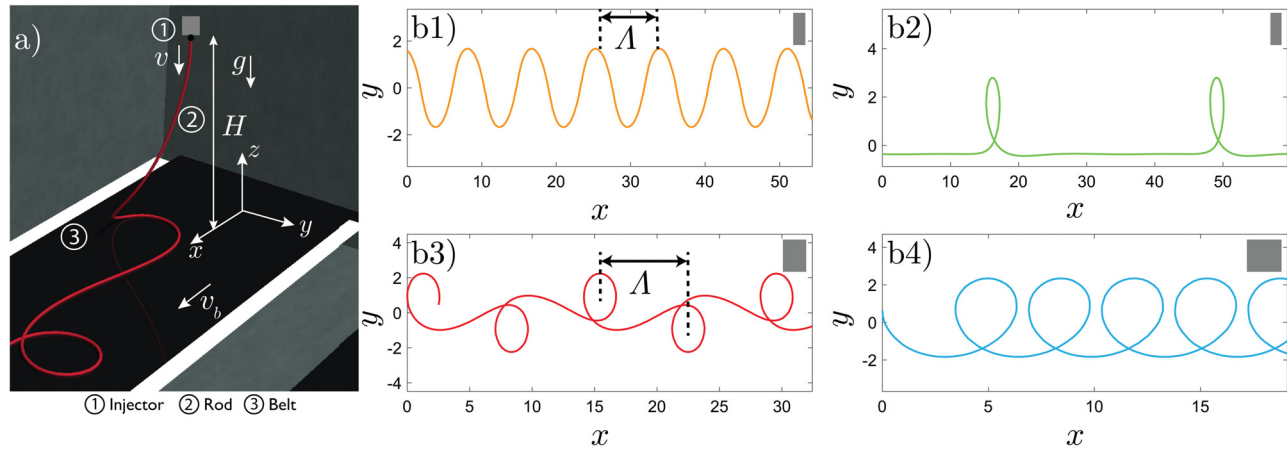
Fig. 1 (*a*) An injector (1) deploys a thin elastic rod (2) onto a conveyor belt (3). (*b*) Representative snapshots of the trace of the rod left on the belt for the various coiling regimes: (1) meanders, $\epsilon=0.25$; (2) stretched coils, $\epsilon=0.18$; (3) alternating loops, $\epsilon=0.55$; and (4) translated coils, $\epsilon=0.75$. The gray rectangles illustrate the relative scales of the *x* and *y* axes.

cm, $\rho = 1.18$ g/cm^3, and $E = 1.3$ MPa (i.e., $L_{gb} = 3.3$ cm) with a belt speed of $v_b \leq 1$ cm/s to ensure a noninertial regime. More details on the material properties can be found in Ref. [3]. Hereafter, we work in units such that $L_{gb} = 1$ and we fix the deployment height at $H = 15$.

In Fig. 1(*b*), we provide representative coiling patterns (trajectories) of the contact point between the rod and the belt: meanders ($0 < \epsilon < 0.56$, Fig. 1(b1)), stretched coils ($0.09 < \epsilon < 0.37$, Fig. 1(b2)), alternating loops ($0.37 < \epsilon < 0.73$, Fig. 1(b3)), and translated coils ($0.67 < \epsilon < 1.00$, Fig. 1(b4)). We showed previously that the phase boundaries between these patterns are set by the dimensionless speed mismatch ϵ, with negligible dependence on L_{gb} and H [2]. When the injection speed is decreased from $v = v_b$ to $v = 0$ (i.e., $\epsilon = 0 \rightarrow 1$), slowly enough for the patterns to reach steady state, the meanders appear first, followed by the alternating loops at $\epsilon = 0.56$, and eventually the translated coils appear at $\epsilon = 0.73$. In the reverse direction of the sweep from $v = 0$ to $v = v_b$ (i.e., $\epsilon = 1 \rightarrow 0$), the sequence is: translated coils, alternating loops, stretched coils, and meanders, with the respective phase boundaries at $\epsilon = \{0.67, 0.37, 0.09\}$. Below, we shall expand further on this pattern classification based on detailed analysis of their Fourier frequency content.

3 Periodicity of Patterns

Despite the variety in the morphology of the patterns, there is universality in the functional dependence of their periodicity on the control parameter ϵ, and on the physical parameters, L_{gb} and H [2]. Consistently with Ref. [2], we define the periodicity length of the patterns Λ, as the distance along $\mathbf{e}_x$ (i.e., the direction of motion of the belt) between the centers of two subsequent coils, or, in case of meanders, between two subsequent extrema (see Fig. 1(*b*)). At a given value of ϵ, the periodicity length can be written as $\Lambda = (D \log (H) + \beta) f(\epsilon)$, where D and β are the numerical constants obtained by data fitting, $f(\epsilon)$ is a function of ϵ only, and we have set $L_{gb} = 1$ in our nondimensionalization scheme. In Ref. [2], we rationalized this behavior based on the shape of the *suspended heel* of the rod near its contact point with the belt (see Sec. 5), prior to buckling. A complete description of Λ then only requires an explanation of its dependence on ϵ, which we did not address in our previous studies.

In Fig. 2, we plot Λ as a function of the control parameter ϵ, along both the increasing ($\epsilon = 0 \rightarrow 1$, open symbols) and decreasing ($\epsilon = 1 \rightarrow 0$, filled symbols) sweep directions. At $\epsilon = 0^+$, the onset of the meandering pattern arises through a Hopf bifurcation with a finite value of Λ [3] at the onset of the instability. In the other limit, when $\epsilon = 1$ is approached (this limit corresponds to coiling on a static surface), Λ decreases toward zero. In the opposite direction of the sweep, starting at $\epsilon = 1$ and decreasing toward

$\epsilon \rightarrow 0$, the behavior is qualitatively different and Λ increases in a divergent fashion until $\epsilon \approx 0.09$. At this point, the meanders reemerge and the values of Λ match again those of the increasing ϵ sweep.

It is interesting to note that despite the transitions into the different patterns as ϵ is varied, the periodicity length remains continuous across the phase boundaries. This finding suggests that there is a length scale intrinsic to the system that plays the primary role. To further probe this length scale, we perform a fast Fourier transform (FFT) analysis of the patterns, which will subsequently form the basis of the GM developed to describe the dependence of Λ on ϵ (Fig. 2).

4 FFT Analysis and Classification of the Coiling Patterns

In the reference frame of the belt, we define the longitudinal and transverse coordinates of the contact point between the rod and the belt as $x_b(t) = x(t) - v_b t$ and $y_b(t) = y(t)$, respectively, where $x(t)$ and $y(t)$ were defined in Fig. 1(*a*). Given the periodic behavior, each of the coiling patterns yields a distinct orbit in this reference frame, as shown in Fig. 3(*a*).

Following a procedure developed previously for the FMSM [15], we characterize these orbits of the patterns on the belt frame by their FFT, which produces the seven qualitatively different
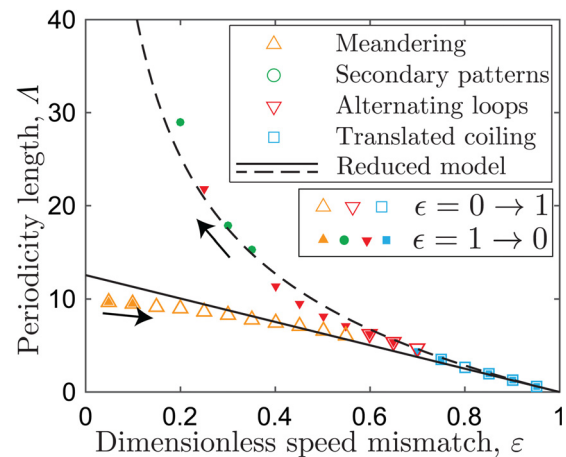

Fig. 2 Periodicity length, Λ, as a function of dimensionless speed mismatch, ϵ. Open (and filled) symbols correspond to the patterns obtained along $\epsilon{=}0{\rightarrow}1$ (and $\epsilon{=}1{\rightarrow}0$) direction. The black solid and dashed lines represent the results from the reduced geometry-based model introduced in Secs. 5 and 6.
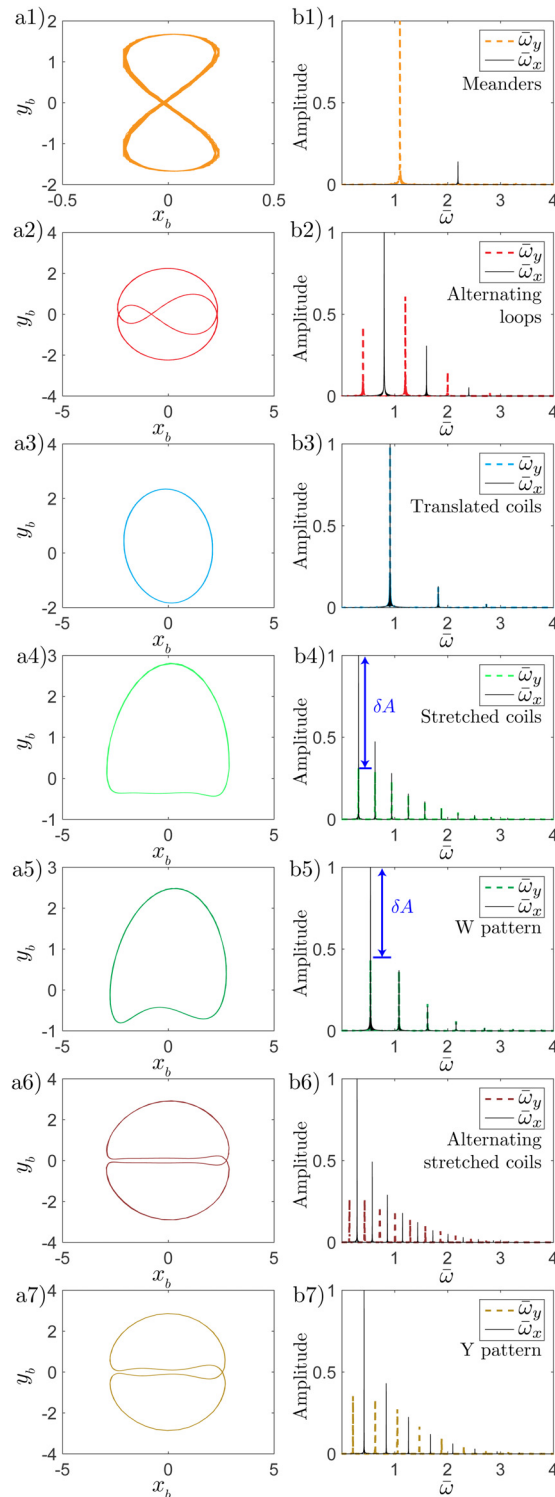
Fig. 3 (*a*) Representative trace of the rod in the belt frame along (x_b, y_b) for each pattern. (*b*) Fourier frequency spectra with amplitude normalized by the largest peak, and frequencies ω, normalized by $\omega_c = v/(2\pi R_c)$, where R_c is the radius of the coil when the belt is static $\varepsilon = 0$. The patterns are: (1) meanders ($\epsilon = 0.25$), (2) alternating loops ($\epsilon = 0.55$), (3) translated coils ($\epsilon = 0.75$), (4) stretched coils ($\epsilon = 0.18$), (5) *W* pattern ($\epsilon = 0.35$), (6) alternating stretched coils ($\epsilon = 0.16$), and (7) *Y* pattern ($\epsilon = 0.24$).

frequency spectra presented in Fig. 3(*b*). The longitudinal and transverse components of the spectra are represented by the solid and dashed lines, respectively. Both the transverse and the longitudinal frequencies, $\bar{\omega}_x = \omega_x/\omega_c$ and $\bar{\omega}_y = \omega_y/\omega_c$, have been

normalized by $\omega_c = v/(2\pi R_c)$, where R_c is the radius of the circular coils obtained when the belt is static ($\epsilon = 0$) [3], such that ω_c is effectively the steady coiling frequency. The FFT amplitude has also been rescaled such that the maximum amplitude is unity. The choice of this nondimensionalization procedure is motivated by the significance of ω_c in the FMSM, with analogous findings for our ESM, briefly addressed next and later described in more detail in Sec. 5.

The formation of circular coils on a static substrate can be compared to the swinging of a pendulum along both the x and y directions, with the same longitudinal and transverse frequency, ω_c. For a moving belt, these frequencies evolve with ϵ (see Sec. 5). Our previous classification scheme [3], based on empirical observations, now needs to be revisited and expanded. The earlier scheme consisted of four patterns—meanders, stretched coils, alternating loops, and translated coils—whereas the new classification mandates seven—meanders, alternating loops, translated coils, stretched coils, alternating stretched coils, *W* patterns, and *Y* patterns. In the phase diagram along ϵ [2], the meanders, alternating loops, and translated coils have uniquely assigned regions, where no other patterns form: $0 < \epsilon < 0.09$, $0.56 < \epsilon < 0.67$, and $0.73 < \epsilon < 1$, respectively. As such, we refer to them as "primary patterns." The remaining four (stretched coils, alternating stretched coils, *W* pattern, and *Y* pattern) appear only in regions of the multistability of the phase diagram and are collectively termed as the "secondary patterns."

In what follows, we identify the distinguishing features for each pattern based on their frequency content. In particular, we focus on the peak frequencies, denoted as $\bar{\omega}_x^i$ and $\bar{\omega}_y^i$ for the longitudinal and transverse directions, respectively, where the integer i is the order of the peak in increasing sequence, e.g., $\bar{\omega}_x^1$ is the first frequency along the longitudinal direction. The ratio of amplitudes for the spectra for $\bar{\omega}_x^i$ and $\bar{\omega}_y^i$, denoted as A^i, will also be considered.

4.1 Primary Coiling Patterns. The primary patterns—meanders, alternating loops, and translated coils—have prominent distinguishing features in the FFT spectra, with a small number of peaks (a maximum of five). The *meanders* (Figs. 3(a1) and 3(b1)) consist of a superposition of one longitudinal and one transverse mode, with $\bar{\omega}_x^1/\bar{\omega}_y^1 = 2$ and an amplitude ratio $A^1 \ll 1$. The *alternating loops* have five main peaks (Figs. 3(a2) and 3(b2)). Two of them, including the peak with the largest amplitude, are along the longitudinal direction, and the remaining three are in the transverse direction. The second and third largest peaks are along the transverse direction and have approximately similar amplitudes. The frequencies of all five peaks are integer multiples of the first peak $\bar{\omega}_y^1$ and can be described as $\bar{\omega}_y^j = (2j-1)\bar{\omega}_y^1$ with $j = 1, 2, 3$, and $\bar{\omega}_x^k = 2k\bar{\omega}_y^1$ with $k = 1, 2$. The *translated coils* are dominated by a single dominant frequency, $\bar{\omega}_x^1 = \bar{\omega}_y^1$, and the ratio of the corresponding amplitudes is $A^1 = 1$ (see Figs. 3(a3) and 3(b3)).

4.2 Secondary Coiling Patterns. The secondary patterns—stretched coils, alternating stretched coils, *W* pattern, and *Y* pattern (see representative traces in Fig. 4)—have at least six distinct peaks in their frequency content. Both the *stretched coils* and the *W patterns* (Figs. 3(a4) and 3(b4) and 3(a5) and (b5), respectively) are dominated by a longitudinal frequency at $\bar{\omega}_x^1 \lesssim 0.5$. A transverse peak exists at the same frequency but with a significantly smaller amplitude, such that $A^1 < 1$. The primary distinguishing feature between the two is the difference between the amplitudes of the transverse and longitudinal motions, δA (see Figs. 3(b4) and 3(b5)). The *W* patterns exhibit an amplitude ratio of $A^1 \approx 0.5$, whereas the stretched coils have $A^1 < 0.5$. Moreover, while the *W* pattern exhibits three main peaks along both the longitudinal and transverse directions, the stretched coils can have five or more. The location of these modes is well described by $\bar{\omega}_x^i = \bar{\omega}_y^i = i\bar{\omega}_y^1$, where i is a positive integer.

Most of the above patterns have counterparts in the FMSM [15], but the *alternating stretched coils* and the *Y patterns* (Figs.
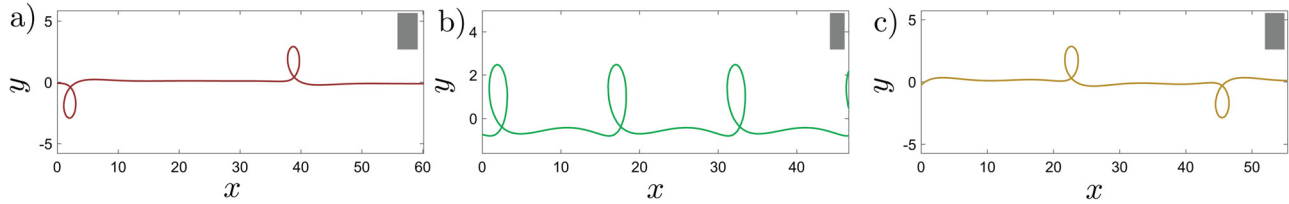
Fig. 4 Traces of secondary patterns from DER: (a) alternating stretched coils ($\epsilon=0.16$), (b) W patterns ($\epsilon=0.35$), and (c) Y patterns ($\epsilon=0.24$). See Fig. 1(b2) for stretched coils. The gray rectangles illustrate the relative scales of the x and y axes.

3(a6) and 3(b6) and 3(a7) and 3(b7), respectively) are unique to the ESM. The first is closely related to the stretched coils, with the only difference being the formation of coils on alternating sides, which does, however, significantly modify the frequency spectrum. The first peak is along longitudinal direction, with amplitude approximately equal to the first longitudinal peak of stretched coils. The peaks are now at $\bar{\omega}_y^i = (2i - 1)\bar{\omega}_y^1$ and $\bar{\omega}_x^i = 2i\bar{\omega}_y^1$ with $i = 1, 2, 3, \ldots$. On the other hand, the Y patterns are the "alternating" analog of the W patterns, and their peaks, although fewer in number, appear at the same locations as those for the alternating stretched coils.

Motivated by this new and detailed analysis of their frequency spectrum, the secondary patterns must be added to the original empirical classification of Refs. [2,3] (shown in Fig. 1(b), above). From the data of our DER simulations, we have established that the stability regions for these new patterns are: $0.14 \le \epsilon \le 0.21$ for the stretched coils, $0.1 \le \epsilon \le 0.17$ for the alternating stretched coils, $0.28 \le \epsilon \le 0.37$ for the W patterns, and $0.21 \le \epsilon \le 0.27$ for the Y patterns. These phase boundaries indicate that there is multistability of more than two distinct patterns at the same value of the control parameter ϵ. A detailed analysis of the nature of this multistability would require a more sophisticated asymptotic numerical continuation method [23] to compute the bifurcations of equilibria and stability of the rod configurations, which is beyond the scope of this paper. Moreover, we note that Ref. [1] reported a number of additional patterns that fall outside of the above classification, which are likely generated due to inertial effects, which are here negligible given the set of parameters used in our study [2].

5 Geometric Description of the Pattern Periodicity

Above, we performed a comprehensive classification of the various coiling patterns based on their frequency content. We now
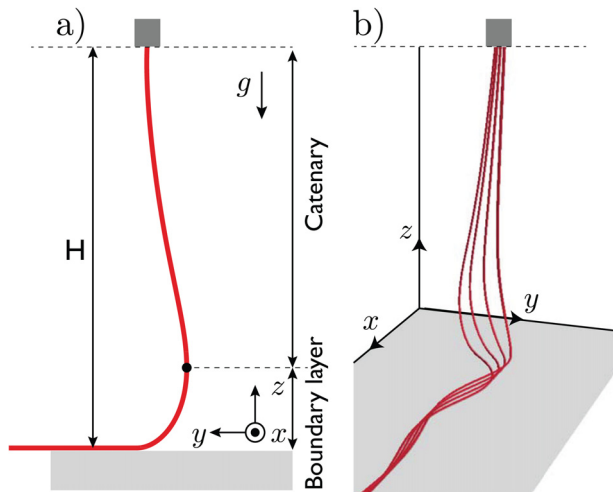

Fig. 5 Schematic diagrams for (a) the suspended heel, comprising a catenary region and a boundary layer; and (b) time-lapsed superposition of the rod configurations, over a quarter period of the meandering patterns

focus on determining the factors that dictate the periodicity of these patterns. In our earlier work [2], we demonstrated that the shape of the *suspended heel* (i.e., the hanging portion of the rod between the injector and the contact point with the belt) sets the length scales of the patterns. This heel can be further divided into a *catenary region* (the nearly straight portion that emanates from the injector) and a *boundary layer region* (the nonlinear part that connects the catenary to the contact point), as shown in the schematic of Fig. 5(a).

The swinging motion of the catenary is essentially pendular with a characteristic amplitude that we assume to be independent of the boundary layer (see schematic in Fig. 5(b), over 1/4th of a time period). Below, this assumption shall be validated against our simulation results. The characteristic amplitude of the swinging motion is set by a natural curvature that is intrinsic to the system geometry governed by both the gravito-bending length, L_{gb}, and the deployment height, H [2]. When the dimensionless speed mismatch, ϵ, between the injection and belt is increased from $\epsilon = 0$ to $\epsilon = 1$, this length scale is excited through a Hopf bifurcation and stays nearly constant as a function of ϵ.

To corroborate the above interpretation, we return to the frequency analysis presented in Sec. 4, where every frequency peak was found to occur at an integer multiple of the lowest peak frequency, and consequently, the wavelength along the belt is set by this frequency. Note that in the cases of the alternating loops, the alternating stretched coils, and the Y patterns, a single period comprises two coils such that the periodicity length is set by twice the lowest peak frequency. Moreover, for all the patterns, the lowest peak frequency is along the transverse (y) direction. It therefore suffices to only consider the ω_y^i peaks to deduce the periodicity length.

In Fig. 6(a), we present a phase diagram of the FFT amplitude on the ($\bar{\omega}_y, \epsilon$) space and observe that the lowest peaks are located at $\omega_c = v/(2\pi R_c)$ (dashed line) for the meanders and the translated coils, and at $\omega_c/2$ for the alternating loops (dotted line). Therefore, all of the patterns obtained in the $\epsilon = 0 \to 1$ sweep direction have a periodicity length of

$$\Lambda = \frac{v_b}{\omega_c} = 2\pi R_c (1 - \epsilon) \tag{1}$$

which is plotted as the solid line in Fig. 2 and is in good agreement with our simulation data.

In the opposite parameter sweep direction ($\epsilon = 1 \to 0$), in addition to the alternating loops and translated coils, we also observe the secondary patterns, earlier described in Sec. 4.2. Eventually, the meanders reappear in a narrow regime, $\epsilon \le 0.09$. Ignoring for now this reentrant meandering regime, we conclude that the patterns in the $\epsilon = 1 \to 0$ sweep are essentially loops connected by catenary-like threads. As ϵ is decreased, the distance between the two loops (as well as Λ) increases. When $\epsilon = 0$, there is no *excess* rod on the belt and the distance between two loops must diverge ($\Lambda \to \infty$). As an approximation and ignoring the narrow meandering regime, we reason heuristically that the lowest peak frequency (and twice of that for alternating loops, alternating stretched coils, and Y pattern) should fall on the modified coiling frequency $\omega_c^* = v/(2\pi R_c)\epsilon^m$, where the exponent m is regarded as a fitting parameter, so that $\bar{\omega}_y^1 \to 0$ in the limit of $\epsilon \to 0$. Let us examine the prediction from this power-law at the two extreme limits: $\epsilon = 1$ and $\epsilon = 0$. The case
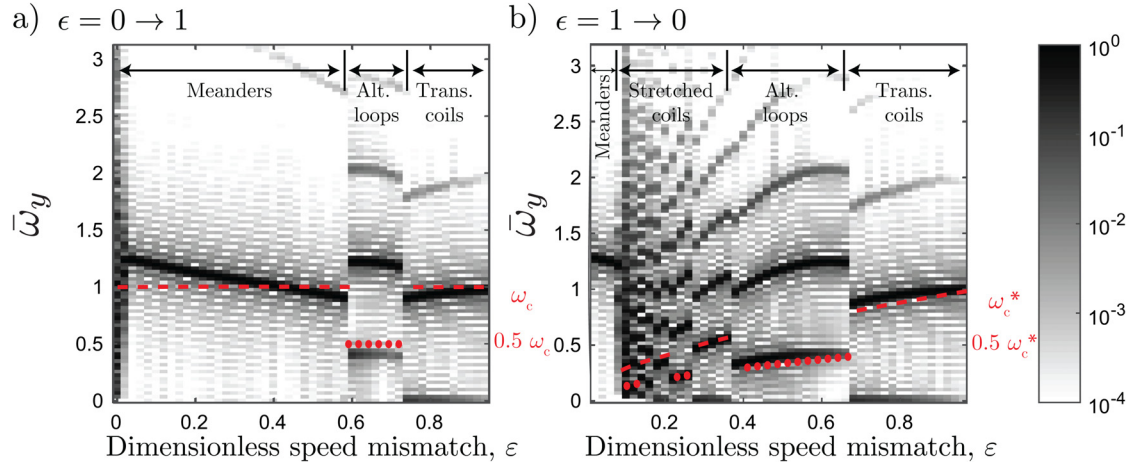
Fig. 6 Phase diagram showing the dependence of the FFT amplitude (adjacent bar) on both the transverse frequencies, ω_y, and the dimensionless speed mismatch, ϵ: (*a*) $\epsilon = 0 \to 1$ and (*b*) $\epsilon = 1 \to 0$. At each value of ϵ, the amplitudes are normalized by the maximum amplitude. The dashed (and dotted) lines correspond to (*a*) ω_c (and $0.5\,\omega_c$) and (*b*) ω_c^* (and $0.5\,\omega_c^*$). For all the patterns, the lowest peak frequency always falls onto either of these lines.

of $\epsilon = 1$ corresponds to the translated coiling regime and the lowest peak frequency is $v/(2\pi R_c)$. This implies that the periodicity length is $\Lambda = 0$, consistently with a circular coil with radius R_c. In the other limit, at $\epsilon = 0$, the lowest peak frequency is zero, and $\Lambda \to \infty$, as required by the construction.

The periodicity length that emerges from this power-law reads

$$\Lambda = 2\pi R_c (1 - \epsilon)\epsilon^{-m} \qquad (2)$$

where $m = 0.57 \pm 0.04$ was obtained from fitting to the data presented in Fig. 2. This prediction is shown in Fig. 2 as a dashed line and agrees well with the simulation data. The prediction from this power-law interpretation for ω_c^* is plotted in Fig. 6(*b*) as a dashed line, which we find to be in good agreement with the lowest peak frequency for meanders, translated coils, stretched coils, and *W* patterns. For the alternating loops, alternating stretched coils, and *Y* patterns, the lowest peak frequency agrees well with $\omega_c^*/2$ (dotted line in Fig. 6(*b*)).

Even if an analytical description of a rod injected onto a belt is beyond the scope of the present study, our numerical analysis provides the following interpretation of the periodic pattern formation process. When the control parameter is increased, $\epsilon = 0 \to 1$, a Hopf bifurcation at $\epsilon = 0^+$ excites an intrinsic radius of curvature of the heel set by the system geometry and is proportional to L_{gb} and $\log(H)$. This results in a pendular swinging motion with a frequency ω_c that remains approximately constant. The periodicity length that derives from this pendulum analogy is given in Eq. (1) and is found to be continuous across the various phase boundaries. In the opposite direction of the parameter sweep, $\epsilon = 1 \to 0$, this periodicity length is required to diverge at $\epsilon = 0$ and the pendulum frequency tends to zero. This results in a different (yet continuous in ϵ) description of periodicity length described in Eq. (2). At a given value of ϵ, Eqs. (1) and (2) indicate that the periodicity length scales with the static coiling radius, $\Lambda \sim R_c$. This static coiling radius has a universal description, $R_c = 0.274 \log(H) + 1.27$, that was previously investigated numerically [2] and semi-analytically [19,20]. This explains how the logarithmic dependence on H and the linear dependence on L_{gb} are propagated into the periodicity length, in addition to any other shape parameter pertinent to the patterns, e.g., meandering amplitude.

6 GM for the Pattern Morphology

Having described the various length scales of the periodic coiling patterns, we turn to rationalize their morphology. For this

purpose, we adapt a GM that was recently introduced for the FMSM [22] to explain the pattern formation when a viscous thread is quasi-statically deposited onto a moving belt. Similarly to our elastic case, the primary ingredient of this GM is the dimensionless difference ϵ, between the belt speed and the terminal velocity at which the hanging thread impacts the belt. This model comprises three coupled ODEs for three state variables of the thread defined in the neighborhood of the contact point between the falling thread and the belt, namely: (i) the radial deflection r, (ii) the orientation of the path of the thread ϕ, and (iii) its curvature κ near the contact point (see schematic in Fig. 7(*a*)) [22]. Under quasi-static conditions (i.e., ignoring inertial effects) and for fixed values of ϵ and H, the full shape of the hanging thread (κ, in particular) is time invariant and set by the current boundary conditions applied to the thread, yielding $\kappa = \kappa(r, \phi)$. In Ref. [22], the curvature of a viscous thread near the contact point $\kappa(r, \phi)$ was obtained by fitting numerical simulations using the discrete viscous rods algorithm (DVR) [14], which leverages similar principles of discrete differential geometry to those of DER.

Given the near identical geometry of the hanging viscous thread in the FMSM and the elastic rod in the ESM, we assume that the above geometric description is appropriate for the elastic case, except that the curvature of the heel near the point of contact $\kappa(r, \phi)$ now needs to be extracted from the DER simulations. Our geometric approach to recover the various patterns of the ESM consists of first calculating (and tabulating) $\kappa(r, \phi)$ from DER and then numerically solving the three underlying ODEs, as we detail next.

In Fig. 7(*a*), we present a schematic diagram that illustrates the various quantities used in the GM to describe the coiling process. The point of contact between the belt and the rod is located at $\mathbf{r}(r, \psi)$, with respect to the origin that is directly underneath the injector, on the belt. Let s be the arc-length along the trace of the pattern; $s = 0$ corresponds to the point that contacted the moving belt at time $t = 0$, and $s = vt$ corresponds to the current point of contact $\mathbf{r}$. The various coiling patterns can be regarded as arising due to the (assumed) no-slip boundary condition between the suspended rod and the belt. This no-slip condition can only be satisfied if the following evolution equation for $\mathbf{r}$ holds [22]:

$$v\mathbf{t} + v_b\mathbf{e}_x = \dot{\mathbf{r}} = v\mathbf{r}' \qquad (3)$$

where prime refers to differentiation with respect to s, i.e., $\mathbf{r}' = \partial_s\mathbf{r}$ and $\dot{\mathbf{r}} = \partial_t\mathbf{r}$.

The dynamical quantities that prescribe the shape of the patterns are the position of the contact point $\mathbf{r}$, and both the tangent
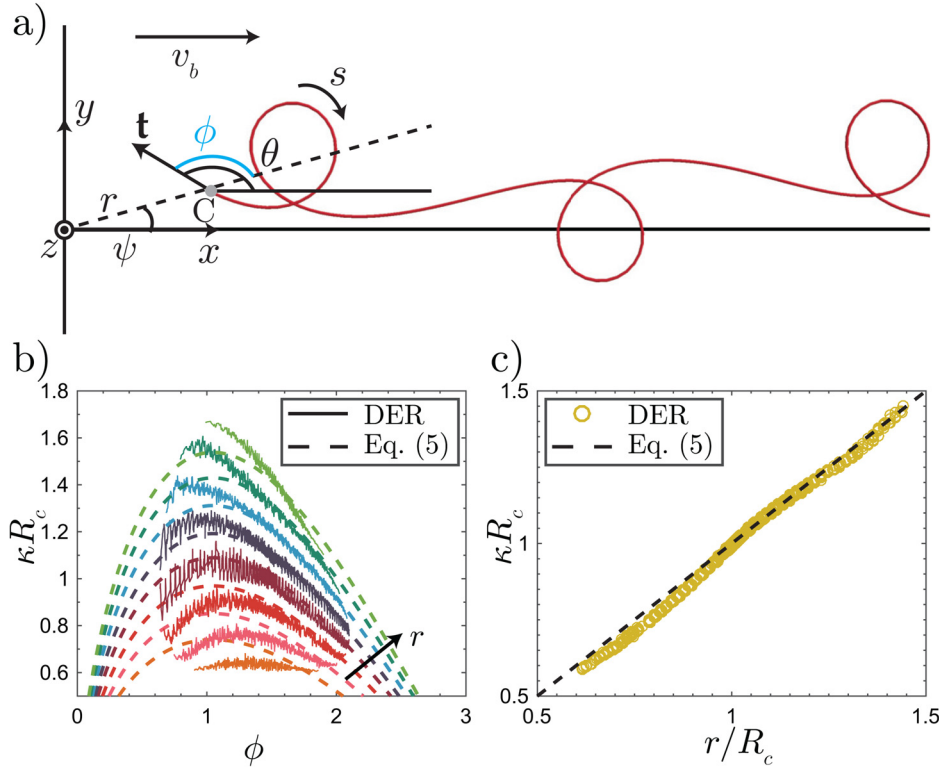
Fig. 7 (*a*) Schematic diagram of the trace of the deposited rod (in the plane of the belt, *x–y*). The rod contacts the belt at the point *C*(r, ψ), with radial distance *r* and polar angle $\psi = \theta - \phi$. The tangent at *C* is t and the curvature of the rod there is $\kappa = \hat{\kappa}(\phi, t, r) = \theta'$. (*b*) Normalized curvature, κR_c, as a function of ϕ calculated from DER (solid line) and the dashed lines were obtained by fitting Eq. (5) to the simulation data, in the range $0.7 < \epsilon < 1.0$. The data were binned for $r/R_c \in [0.7, 1.3]$ in steps of 0.1. (*c*) Dependence of κ on the normalized radius, r/R_c, at $\phi = \pi/2$.

vector **t**, and the curvature κ, at **r** (see Fig. 7(*a*)). The position vector **r** can be described in polar coordinates $(r(s), \psi(s))$, and the unit tangent **t** is given by the angle θ that it makes with the horizontal, such that the curvature at **r** is $\kappa = \theta'$. The quantities r, ψ, θ evolve according to Eq. (3), coupled with κ. Recasting Eq. (3) in a polar basis yields the following complete set of nonlinear ODEs [22], which describes our problem:

$$r' = \cos(\theta - \psi) + (1 - \epsilon)\cos\psi$$
$$r\psi' = \sin(\theta - \psi) - (1 - \epsilon)\sin\psi \qquad (4)$$
$$\theta' = \kappa(r, \theta - \psi)$$

where under the assumption of quasi-static conditions, κ is taken only as a function of the radial coordinate r, of the contact point and the polar angle $\phi = \theta - \psi$, of the tangent. To close our GM, we need the functional form of κ, which we obtain by fitting the DER simulation data over the range $0.7 < \epsilon < 1.0$ along $\epsilon = 1 \rightarrow 0$ to:

$$\kappa(r, \phi) = A \frac{r}{R_c^2} \sin\left(\pi\left[\frac{\phi}{\pi}\right]^\alpha\right) \qquad (5)$$

where α is a fitting parameter. To determine the other parameter A, we consider the limiting case of deployment onto a static belt ($\epsilon = 1$), which produces circular coils of radius $r = R_c$ [3]. In this limit, the curvature at the contact point is $\kappa = 1/R_c$ and $A = 1/\sin(\pi/2^\alpha)$. Therefore, our model has a single fitting parameter, α.

The specific form of Eq. (5) was chosen heuristically, motivated by the hypothesis that the effects of r and ϕ are separable. We

were also encouraged by the simplicity of the resulting physical picture, as well as by its success at describing the data, albeit at the expense of accuracy. To further corroborate this choice, in Fig. 7(*b*), we plot κ as a function of ϕ in the range $r/R_c \in [0.7, 1.3]$, at discrete steps of 0.1, and obtain $\alpha = 0.631 \pm 0.001$ by fitting the data to Eq. (5). It remains to show that $\kappa \sim r/R_c^2$ at a fixed value of ϕ, which can be interpreted using the following physical argument. As the radial deflection of the contact point increases, its curvature must increase appropriately (we assume in a linearly proportional way) so that the heel can remain in a closed orbit revolving around the projection of the injector on the belt. In Fig. 7(*c*), we plot κR_c as a function of r/R_c, while fixing $\phi = \pi/2$, and find that the DER data are well described by $\kappa(r, \pi/2) = r/R_c^2$, in accordance with Eq. (5) and confirming the above linear assumption between the curvature at the contact point and the radial deflection.

The set of ODEs in Eq. (4) can be readily integrated numerically with minimal computation time (typically under 1 s using Mathematica running on a 2.6 GHz Intel Core i7 processor). Through this integration of our GM, we have been able to reproduce all of the patterns obtained in DER, which were presented in Secs. 2 and 4 (shown in Figs. 1 and 4), except some of the secondary patterns, namely: stretched coils, alternating stretched coils, and the *Y* patterns. We attribute the fact that the GM is unable to reproduce some of the coiling patterns to the approximations made in the fitting procedure for the function $\kappa(r, \phi)$, including the fact that the explicit effect of twist was neglected. Nonetheless, it is important to highlight that the shape of the patterns is recovered almost exactly. In Fig. 8, we contrast representative traces of the patterns obtained from the DER simulation with those predicted by our model, finding excellent agreement between the two. Moreover, the GM is able to capture the
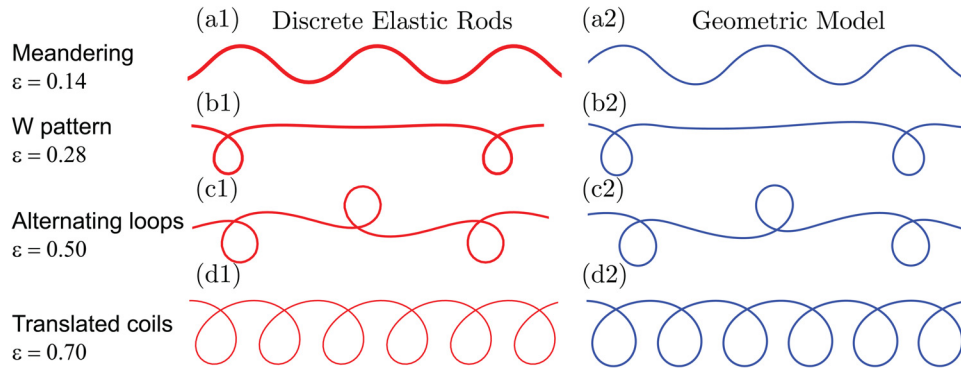
Fig. 8 Comparison of traces between (1) DER simulations and (2) the GM: (*a*) meanders (ε=0.14), (*b*) *W* patterns (ε=0.28), (*c*) alternating loops (ε=0.50), and (*d*) translated coils (ε=0.70)

variation in the pattern shape as a function of the control parameter, ϵ, e.g., the meandering amplitude increases with ϵ.

The GM can now be used to evaluate the critical values of ϵ at which transitions between patterns occur. In Fig. 9(*a*), we compare the regions of stability for the various patterns as a function of the dimensionless speed mismatch, ϵ, obtained from both the DER and the GM. We find that the GM recovers the patterns in the correct order. In the $\epsilon = 0 \rightarrow 1$ direction, meanders, alternating loops, and translated coils appear sequentially. In the reverse direction, the ordering changes to translated coils, alternating loops, secondary patterns, and meanders. Note that all of the single-stable and multistable regimes are well represented by the GM. Meanders, alternating loops, and translated coils have their unique regions of existence along ϵ axis. There are three multistable regimes for (i) meanders and alternating loops, (ii) meanders and secondary patterns, and (iii) alternating loops and translated coils—all well captured by the GM. The excellent agreement in these various features of the pattern formation process provides further support for the reduced physical ingredients used to derive

the GM, and, in particular, the relevance of the radius of coiling R_c, which is the only nongeometrical quantity that enters in the model.

7 Comparison With the FMSM

Thus far, we have focused our investigation on the ESM, toward rationalizing the pattern formation process. Note, however, that in the GM, we did not allude to a specific constitute law and based our description purely on geometry (except for the description of R_c, which essentially sets the length scale of the problem). Similar findings have been reported for the viscous coiling counterpart, the FMSM [22]. This calls for a quantitative comparison of the pattern formation process in the ESM and the FMSM. For this comparison, addressed next, we ignore inertial effects and consider the patterns formed in the visco-gravitational regime of the FMSM.

In Fig. 9(*b*), we show the regimes of existence of the various patterns in noninertial FMSM obtained from DVR simulations and the GM, both of which were calculated in Ref. [22]. The patterns in the fluid and elastic cases are not only similar but also they appear in the same order along both $\epsilon = 0 \rightarrow 1$ and $\epsilon = 1 \rightarrow 0$ directions of the sweep. This further emphasizes the geometric connection between the two systems. The number of single-stable and multistable regimes along ϵ is the same in both the ESM and FMSM, the only difference being an additional tristable regime of meanders, secondary patterns (*W* pattern in this case), and alternating loops in the FMSM, that does not have a counterpart in the FMSM. This tristable regime appears only in the GM for the FMSM (not in the DVR simulations) and was not previously reported in the fluid case.

Finally, we quantitatively compare the boundaries of the regions of stability for the various patterns in both systems, using the values obtained from DVR simulations for the FMSM (and DER simulations of the ESM). Meanders appear for $0 < \epsilon < 0.51$ (versus $0 < \epsilon < 0.56$), secondary patterns for $0.23 < \epsilon < 0.36$ (versus $0.09 < \epsilon < 0.37$), alternating loops for $0.36 < \epsilon < 0.65$ (versus $0.37 < \epsilon < 0.73$), and translated coils for $0.57 < \epsilon < 1.0$ (versus $0.67 < \epsilon < 1.0$). The quantitative agreement between these two physically distinct systems is remarkable, which places the constitutive details (viscous threads versus elastic rods) on a second pane and highlights the important roles played by geometry and kinematics in both of these problems.

8 Conclusion

We have reported results from a numerical investigation on the ESM and introduced a GM to rationalize the various coiling patterns that it can generate. We established that the wavelength of these patterns is dictated by a single characteristic length that is intrinsic to the shape of the rod in the neighborhood of its point of
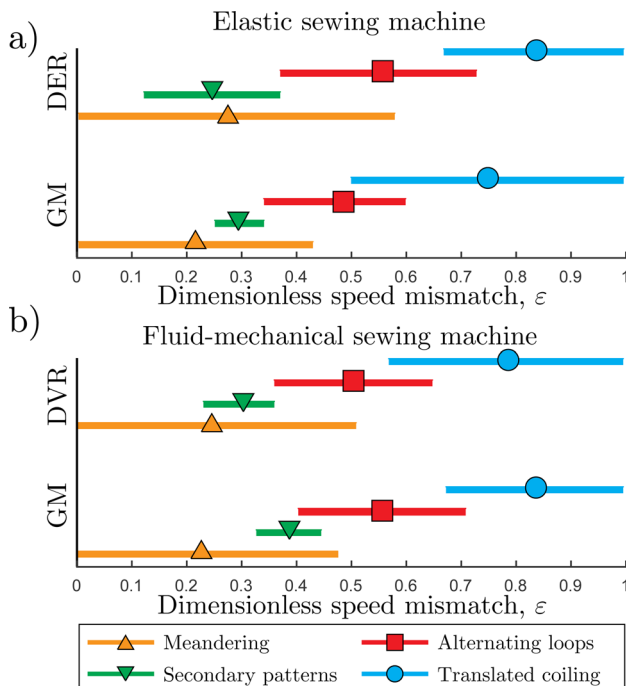

Fig. 9 Regimes of stability of the patterns along ϵ for (*a*) the ESM from the DERs simulations and the GM and (*b*) the FMSM from the DVRs simulations and the corresponding GM for the viscous system [22]

contact with the substrate. This helped us better understand the dependence of the length scales of the patterns on both the gravito-bending length and the deployment height, which was previously reported empirically in Ref. [2]. We also introduced a reduced GM that is able to reproduce the main features of the system, including the morphology of most of the patterns, and their location in the phase diagram.

Finally, we compared our results for the coiling of an elastic rod (ESM) with the fluid counterpart with a viscous thread (FMSM) and demonstrated how geometry is prominent in both systems, despite the significant differences in their constitutive descriptions. Having uncovered fundamental similarities between the two systems, we believe that a significant body of knowledge may now be ported from the case of viscous coiling, which has been more extensively studied in the literature, into the elastic system. In addition, we anticipate that our GM will be useful in better understanding other system with similar geometries, albeit with different constitutive details, such as pattern formation by electrospinning [24] and direct ink-writing 3D printing [25,26].

Acknowledgment

References

[1] Habibi, M., Najafi, J., and Ribe, N. M., 2011, "Pattern Formation in a Thread Falling Onto a Moving Belt an Elastic Sewing Machine," Phys. Rev. E, **84**(1), p. 016219.
[2] Jawed, M. K., and Reis, P. M., 2014, "Pattern Morphology in the Elastic Sewing Machine," Extreme Mech. Lett., **1**, pp. 76–82.
[3] Jawed, M. K., Da, F., Joo, J., Grinspun, E., and Reis, P. M., 2014, "Coiling of Elastic Rods on Rigid Substrates," Proc. Natl. Acad. Sci. U. S. A., **111**(41), pp. 14663–14668.
[4] Gerwick, B. C., 1987, *Construction of Offshore Structures*, Wiley, New York.
[5] Geblinger, N., Ismach, A., and Joselevich, E., 2008, "Self-Organized Nanotube Serpentines," Nat. Nanotechnol., **3**(4), pp. 195–200.
[6] Chiu-Webster, S., and Lister, J., 2006, "The Fall of a Viscous Thread Onto a Moving Surface: A Fluid-Mechanical Sewing Machine," J. Fluid Mech., **569**, pp. 89–111.
[7] Mahadevan, L., Ryu, W. S., and Samuel, A. D., 1998, "Fluid 'Rope Trick' Investigated," Nature, **392**(6672), p. 140.
[8] Maleki, M., Habibi, M., Golestanian, R., Ribe, N., and Bonn, D., 2004, "Liquid Rope Coiling on a Solid Surface," Phys. Rev. Lett., **93**(21), p. 214502.
[9] Morris, S. W., Dawes, J. H., Ribe, N. M., and Lister, J. R., 2008, "Meandering Instability of a Viscous Thread," Phys. Rev. E, **77**(6), p. 066218.
[10] Welch, R. L., Szeto, B., and Morris, S. W., 2012, "Frequency Structure of the Nonlinear Instability of a Dragged Viscous Thread," Phys. Rev. E, **85**(6), p. 066209.
[11] Tchavdarov, B., Yarin, A., and Radev, S., 1993, "Buckling of Thin Liquid Jets," J. Fluid Mech., **253**, pp. 593–615.
[12] Cruickshank, J., and Munson, B., 1981, "Viscous Fluid Buckling of Plane and Axisymmetric Jets," J. Fluid Mech., **113**, pp. 221–239.
[13] Hlod, A., Aarts, A., van de Ven, A., and Peletier, M., 2007, "Mathematical Model of Falling of a Viscous Jet Onto a Moving Surface," Eur. J. Appl. Math., **18**(06), pp. 659–677.
[14] Audoly, B., Clauvelin, N., Brun, P.-T., Bergou, M., Grinspun, E., and Wardetzky, M., 2013, "A Discrete Geometric Approach for Simulating the Dynamics of Thin Viscous Threads," J. Comput. Phys., **253**, pp. 18–49.
[15] Brun, P.-T., Ribe, N. M., and Audoly, B., 2012, "A Numerical Investigation of the Fluid Mechanical Sewing Machine," Phys. Fluids, **24**(4), p. 043102.
[16] Ribe, N. M., Lister, J. R., and Chiu-Webster, S., 2006, "Stability of a Dragged Viscous Thread: Onset of 'Stitching' in a Fluid-Mechanical Sewing Machine," Phys. Fluids, **18**(12), p. 124105.
[17] Bergou, M., Audoly, B., Vouga, E., Wardetzky, M., and Grinspun, E., 2010, "Discrete Viscous Threads," ACM Trans. Graphics, **29**(4), p. 116.
[18] Ribe, N. M., 2004, "Coiling of Viscous Jets," Philos. Trans. R. Soc. London, Ser. A, **460**(2051), pp. 3223–3239.
[19] Mahadevan, L., and Keller, J. B., 1996, "Coiling of Flexible Ropes," Philos. Trans. R. Soc. London, Ser. A, **452**(1950), pp. 1679–1694.
[20] Habibi, M., Ribe, N., and Bonn, D., 2007, "Coiling of Elastic Ropes," Phys. Rev. Lett., **99**(15), p. 154302.
[21] Bergou, M., Wardetzky, M., Robinson, S., Audoly, B., and Grinspun, E., 2008, "Discrete Elastic Rods," ACM Trans. Graphics, **27**(3), p. 63.
[22] Brun, P.-T., Audoly, B., Ribe, N. M., Eaves, T. S., and Lister, J. R., 2015, "Liquid Ropes: A Geometrical Model for Thin Viscous Jet Instabilities," Phys. Rev. Lett., **114**, p. 174501.
[23] Lazarus, A., Miller, J., and Reis, P., 2013, "Continuation of Equilibria and Stability of Slender Elastic Rods Using an Asymptotic Numerical Method," J. Mech. Phys. Solids, **61**(8), p. 1712.
[24] Xin, Y., and Reneker, D. H., 2012, "Hierarchical Polystyrene Patterns Produced by Electrospinning," Polymer, **53**(19), pp. 4254–4261.
[25] Lewis, J. A., Smay, J. E., Stuecker, J., and Cesarano, J., 2006, "Direct Ink Writing of Three-Dimensional Ceramic Structures," J. Am. Ceram. Soc., **89**(12), pp. 3599–3609.
[26] Passieux, R., Guthrie, L., Rad, S. H., Lévesque, M., Therriault, D., and Gosselin, F. P., 2015, "Instability-Assisted Direct Writing of Microstructured Fibers Featuring Sacrificial Bonds," Adv. Mater., **27**(24), pp. 3676–3680.